


## Article

# Highly Dispersed Mn–Ce Binary Metal Oxides Supported on Carbon Nanofibers for Hg<sup>0</sup> Removal from Coal-Fired Flue Gas

Yongjun Xia <sup>1</sup>, Zhiqiang Liao <sup>2,3</sup>, Yan Zheng <sup>4</sup> and Zijian Zhou <sup>2,\*</sup> 

<sup>1</sup> State Grid Jiangxi Electric Power Science Research Institute, Nanchang 330096, China; 2008984104@nit.edu.cn

<sup>2</sup> State Key Laboratory of Coal Combustion, School of Energy and Power Engineering, Huazhong University of Science & Technology, Wuhan 430074, China; m201771050@hust.edu.cn

<sup>3</sup> Chongqing Sanfeng Environment Group Co., Ltd., Chongqing 400084, China

<sup>4</sup> Nanchang Institute of Technology, Nanchang 330099, China; 357104216005@email.ncu.edu.cn

\* Correspondence: zhouzj\_sklcc@hust.edu.cn; Tel.: +86-27-87542417; Fax: +86-27-87545526

Received: 30 October 2018; Accepted: 4 December 2018; Published: 5 December 2018



**Abstract:** Highly dispersed Mn–Ce binary metal oxides supported on carbon nanofibers (MnO<sub>x</sub>–CeO<sub>2</sub>/CNFs(OX)) were prepared for Hg<sup>0</sup> removal from coal-fired flue gas. The loading value of the well-dispersed MnO<sub>x</sub>–CeO<sub>2</sub> was much higher than those of many other reported supports, indicating that more active sites were loaded on the carbon nanofibers. In the present study, 30 wt % metal oxides (15 wt % MnO<sub>x</sub> and 15 wt % CeO<sub>2</sub>) were successfully deposited on the carbon nanofibers, and the sorbent yielded the highest Hg<sup>0</sup> removal efficiency (>90%) within 120–220 °C under a N<sub>2</sub>/O<sub>2</sub> atmosphere. An increase in the amount of highly dispersed metal oxides provided abundant active species for efficient Hg<sup>0</sup> removal, such as active oxygen species and Mn<sup>4+</sup> cations. Meanwhile, the carbon nanofiber framework provides the pathway for charge transfer during the heterogeneous Hg<sup>0</sup> capture reaction processes. Under a N<sub>2</sub>+6%O<sub>2</sub> atmosphere, a majority of Hg<sup>0</sup> was removed via chemisorption reactions. The effects of flue gas composition were also investigated. O<sub>2</sub> replenished the active oxygen species on the surface and thus greatly promoted the Hg<sup>0</sup> removal efficiency. SO<sub>2</sub> had an inhibitory effect on Hg<sup>0</sup> removal, but NO facilitated Hg<sup>0</sup> capture performance. Overall, carbon nanofibers seems to be a good candidate for the support and MnO<sub>x</sub>–CeO<sub>2</sub>/CNFs(OX) may be promising for Hg<sup>0</sup> removal from coal-fired flue gas.

**Keywords:** coal-fired flue gas; mercury; carbon nanofibers; metal oxides; adsorption

## 1. Introduction

Mercury (Hg) pollution has attracted worldwide concern because Hg and its compounds cause serious damage to human health and the environment [1]. Coal-fired power plants account for 24% of global anthropogenic mercury emissions, but mercury emitted from power plants has not been controlled efficiently until recent years [2,3]. In coal-fired flue gas, Hg always exists in three forms: oxidized (Hg<sup>2+</sup>), particulate-bounded (Hg<sup>P</sup>), and elemental (Hg<sup>0</sup>) mercury [4,5]. Among them, Hg<sup>P</sup> could be captured along with the fly ash by dust removal devices (electrostatic precipitators or fabric filters), and water-soluble Hg<sup>2+</sup> could be removed by wet flue gas desulfurization devices [6,7]. However, Hg<sup>0</sup> in the flue gas is difficult to control; thus, Hg<sup>0</sup> is the dominant species emitted to the atmosphere. To remove Hg<sup>0</sup>, adsorption and catalytic oxidation technologies have been proposed. Many materials, such as activated carbon [8,9], have been used for Hg<sup>0</sup> adsorption, but the poor selectivity and high cost have limited large-scale application. In recent years, much attention has been paid to sorbents based on transition metal oxides. The transition metal oxides exhibit excellent

performances for  $\text{Hg}^0$  capture due to their extraordinary properties of multiple valence states and high chemical stability.  $\text{VO}_x$  [10,11],  $\text{CoO}_x$  [12],  $\text{CuO}_x$  [13], and  $\text{FeO}_x$  [14], etc., have been investigated for  $\text{Hg}^0$  removal in simulated coal-fired flue gas. However, the  $\text{Hg}^0$  removal efficiencies of these transition metal oxides greatly rely on the concentration of HCl in the flue gas [5,14]. When there is little HCl in the flue gas, the  $\text{Hg}^0$  removal activity of the above sorbents will be limited [15]. Therefore, it is essential to develop transition-metal-oxide-based sorbents for efficient  $\text{Hg}^0$  removal in flue gas with a low HCl concentration or in the absence of HCl.

$\text{MnO}_x$ -supported sorbents may be a promising candidate for  $\text{Hg}^0$  removal even in the absence of HCl [16]. In our previous study, we found that chemically adsorbed oxygen species were mainly responsible for the low-temperature activity of  $\text{MnO}_x$  in the absence of HCl [17].  $\text{O}_2$  in the flue gas is an important component to promote the  $\text{Hg}^0$  removal activity because it can replenish the active oxygen species of the sorbents which are consumed in the  $\text{Hg}^0$  adsorption reactions [18]. In addition, the  $\text{O}_2$  concentration in flue gas is much higher than that of HCl, so making full use of  $\text{O}_2$  to remove  $\text{Hg}^0$  is of significance. Hence,  $\text{CeO}_2$  has been widely used to modify the metal oxides to enhance their  $\text{Hg}^0$  removal activity due to its large oxygen storage capacity [18].  $\text{Ce}^{3+}$  cations could yield charge imbalance, vacancies, and unsaturated chemical bonds, which lead to an increase of the chemisorbed oxygen concentration on its surface [19,20]. In the  $\text{Ce}^{4+}/\text{Ce}^{3+}$  redox couple,  $\text{CeO}_2$  loses the active oxygen to oxidize the cations with low valence and/or  $\text{Hg}^0$ , which then turn into  $\text{Ce}_2\text{O}_3$ . Meanwhile,  $\text{Ce}_2\text{O}_3$  adsorbs  $\text{O}_2$  and turns into  $\text{CeO}_2$ , which achieves the use of  $\text{O}_2$  in flue gas [19].

Up to today,  $\text{MnO}_x$ - $\text{CeO}_2$  binary metal oxides have been used for  $\text{Hg}^0$  removal in a few investigations. As far as is known,  $\text{MnO}_x$ - $\text{CeO}_2$  mixed oxides supported on  $\text{TiO}_2$  [19,21], Ti-PILCs [16], activated coke [22], and  $\gamma\text{-Al}_2\text{O}_3$  [23] for  $\text{Hg}^0$  removal have been reported. These sorbents exhibited good  $\text{Hg}^0$  removal performance. However, the results also showed that with increasing active metal oxide loading, the metal oxides tend to agglomerate, leading to an insufficient use of active metal oxides. In addition, the conductivity of  $\text{MnO}_x$  particles on these supports is poor, thus limiting their efficiency. Therefore, a novel highly dispersed  $\text{MnO}_x$ - $\text{CeO}_2$ -based sorbent still needs to be investigated.

The use of carbon-based materials as sorbent supports could enhance the conductivity of the metal oxides. Carbon nanofibers are graphene-like nanomaterials with large specific surface area and surface nano-effect, so the metal oxides are easily loaded and dispersed. The conductivity of carbon nanofibers is very good because of their high graphitization degree [24]. During the  $\text{Hg}^0$  oxidation process,  $\text{Hg}^0$  loses two electrons, and a lot of electrons shift between the  $\text{Mn}^{4+}/\text{Mn}^{3+}$  and  $\text{Ce}^{4+}/\text{Ce}^{3+}$  electronic couples [25]. The metal oxides are highly dispersed on the nanofibers and the  $\text{Hg}^0$  will be captured by the well-dispersed active species. In this process, carbon nanofibers will act well as charge transfer channels. Besides this, oxidation treatment of the carbon nanofibers would increase the amount of oxygen-containing functional groups, which contribute to the dispersion and anchoring of active metals. Therefore, oxidized carbon nanofibers may be an ideal support to load more highly dispersed  $\text{MnO}_x$ - $\text{CeO}_2$  composites.

In this work, carbon nanofibers were firstly pretreated using  $\text{HNO}_3$ . Then, the  $\text{MnO}_x$  and  $\text{CeO}_2$  were loaded on the treated carbon nanofibers by a wet chemistry method. The influences of loading values, reaction temperatures, and individual flue gas components were investigated. The  $\text{Hg}^0$  removal mechanism of the novel sorbent was also studied.

## 2. Material and Methods

### 2.1. Sorbent Preparation and Characterization

The material preparation and characterization are described in the Supporting Information (Sections 1 and 2). The synthesized sorbents were named  $\alpha\text{MnO}_x$ - $\alpha\text{CeO}_2/\text{CNFs}(\text{OX})$ , where  $\alpha$  represents the mass percentage of  $\text{MnO}_2$  and  $\text{CeO}_2$  in the sorbents. The mass ratio of Mn/Ce was set to 1:1. Five sorbents with different loading values ( $\alpha = 6\%$ ,  $9\%$ ,  $12\%$ ,  $15\%$ , and  $18\%$ ) were prepared.

## 2.2. Experimental

The  $\text{Hg}^0$  removal activity was tested on a lab-scale fixed-bed reactor [17]. A mercury permeation tube was used to generate constant  $\text{Hg}^0$ . The sorbent was packed in a 10 mm inner diameter quartz tube reactor. The  $\text{Hg}^0$  concentration was monitored by an RA-915M mercury analyzer (LUMEX, St. Petersburg, Russia). In each test, the total gas flow rate was 1000 mL/min, and the mass of the sorbent was 0.2 g. The  $\text{Hg}^0$  concentration in the simulative flue gas was  $\sim 95 \mu\text{g}\cdot\text{m}^{-3}$ . The detailed experimental conditions are shown in Table S1.

In this study, the  $Q/M$  ( $Q$  represents flow rate of the simulative flue gas;  $M$  represents sorbent mass) value was  $300,000 \text{ mL}\cdot\text{h}^{-1}\cdot\text{g}^{-1}$ . The  $\text{Hg}^0$  removal efficiency in this study was defined using Equation (1):

$$\eta = (\text{Hg}_{in}^0 - \text{Hg}_{out}^0) / \text{Hg}_{in}^0 \times 100\% \quad (1)$$

in which  $\text{Hg}_{in}^0$  and  $\text{Hg}_{out}^0$  represent the  $\text{Hg}^0$  concentrations upstream and downstream of the sorbent bed, respectively, in  $\mu\text{g}\cdot\text{m}^{-3}$ .

## 3. Results and Discussion

### 3.1. Sorbent Characterization

The surface physical characteristics of the samples are shown in Table 1. The BET specific surface area of CNFs(OX) was higher than that of the raw commercial nanofibers ( $89.512 \text{ m}^2/\text{g}$ ). This suggested that the ultrasonic oxidation treatment of the commercial nanofibers resulted in an increase of the specific surface area. This may be owing to the removal of ash on the commercial nanofibers' surface during the ultrasonic oxidation treatment process. Meanwhile, the treatment process may also enrich surface defects. As shown in Table 1, the BET surface area and average pore volume decreased continuously as the loading value increased from 6% to 18%. This phenomenon indicates that metals entered the pore channels of CNFs(OX).

**Table 1.** The surface physical characteristics of different adsorbents.

| $\alpha$ | Specific Surface Area ( $\text{m}^2/\text{g}$ ) | Pore Volume ( $\text{cm}^3/\text{g}$ ) |
|----------|-------------------------------------------------|----------------------------------------|
| 0        | 96.532                                          | 0.461                                  |
| 6%       | 97.020                                          | 0.350                                  |
| 9%       | 93.853                                          | 0.299                                  |
| 12%      | 88.948                                          | 0.307                                  |
| 15%      | 87.158                                          | 0.293                                  |
| 18%      | 86.729                                          | 0.286                                  |

The  $\text{Hg}^0$  removal process over the transition metal oxides consists of typical heterogeneous redox reactions, so the details of the surface properties of the sorbents are very significant. The surface atomic concentrations of the different samples are summarized in Table 2. The surface oxygen concentration of CNFs was 2.59%. As shown in Table 2, the surface oxygen concentration increased to 3.24% after ultrasonic oxidation treatment. Six different oxygen species were fitted to O 1s XPS spectra, as shown in Figure 1a–c. As seen in Figure 1a,b, the proportion of oxygen-containing functional groups C=O or –OH in esters and anhydrides (532.3–532.8 eV) [26] increased from 34.01% to 44.15% after the ultrasonic oxidation treatment of the CNFs. Meanwhile, the proportion of –COOH (534.3–535.4 eV) [26] increased from 4.46% to 4.80%. The increase in oxygen-containing functional groups, especially –COOH, would facilitate the dispersion and anchoring of active metals. Besides this, as seen from Table 2, the surface oxygen atom concentration increased constantly with increasing  $\text{MnO}_x$  and  $\text{CeO}_2$  loading values, which was assigned to oxygen species in the metal oxides.

**Table 2.** Surface atomic concentration of the adsorbents based on XPS results.

| $\alpha$ | Surface Atomic Concentration (%) |       |       |                                    |       |                                    |
|----------|----------------------------------|-------|-------|------------------------------------|-------|------------------------------------|
|          | C 1s                             | O 1s  | Mn 2p | Mn <sup>4+</sup> /Mn <sup>3+</sup> | Ce 3d | Ce <sup>3+</sup> /Ce <sup>4+</sup> |
| 0        | 96.76                            | 3.24  |       |                                    |       |                                    |
| 6%       | 96.31                            | 2.98  | 0.48  | 0.4277                             | 0.23  | 0.5523                             |
| 9%       | 91.28                            | 6.28  | 1.61  | 0.4212                             | 0.83  | 0.3174                             |
| 12%      | 90.24                            | 6.94  | 1.88  | 0.4171                             | 0.94  | 0.2900                             |
| 15%      | 85.98                            | 9.74  | 2.85  | 0.4140                             | 1.43  | 0.2859                             |
| 18%      | 79.95                            | 13.12 | 3.64  | 0.3218                             | 1.85  | 0.2734                             |

The surface Mn and Ce atomic concentrations also increased constantly with increasing Mn and Ce loading values. As shown in Figure 1d, two orbits of the Mn 2p XPS spectra belong to Mn 2p<sub>1/2</sub> (~653.8 eV) and Mn 2p<sub>3/2</sub> (~642.2 eV). Mn 2p<sub>3/2</sub> can be fitted to three subpeaks: Mn<sup>3+</sup> (~641.8 eV), Mn<sup>4+</sup> (~643.5 eV) [16], and satellites (~646.1 eV) [27]. Mn<sup>4+</sup> species are recognized as the most important active component for Hg<sup>0</sup> oxidation. Although the ratio of Mn<sup>4+</sup>/Mn<sup>3+</sup> decreased slightly with increasing loading value, the absolute amount of Mn<sup>4+</sup> ions still increased with increasing loading value except for 18%MnO<sub>x</sub>-18%CeO<sub>2</sub>/CNFs(OX). Figure 1e shows the Ce 3d XPS spectra of fresh 15%MnO<sub>x</sub>-CeO<sub>2</sub>/CNFs(OX). The Ce 3d XPS spectra could be fitted into eight subpeaks [28]. Among them, v/u, v2/u2, and v3/u3 belong to Ce<sup>4+</sup>, while v1/u1 belongs to Ce<sup>3+</sup>. Ce<sup>3+</sup> species are considered to be important for the catalytic oxidation and adsorption of Hg<sup>0</sup> [29], because Ce<sup>3+</sup> could lead to a charge imbalance, which facilitates Hg<sup>0</sup> oxidation process as more active oxygen species yield. As shown in Table 3, the absolute amount of Ce<sup>3+</sup> cations also increased with increasing CeO<sub>2</sub> loading value. From the XPS characterization results, with the increase of the highly dispersed Mn and Ce loading, MnO<sub>x</sub>-CeO<sub>2</sub>/CNFs(OX) sorbents offered abundant active oxygen, Mn<sup>4+</sup>, and Ce<sup>3+</sup> species. They play important roles in promoting the Hg<sup>0</sup> removal activity. In addition, the electron pairs of Mn<sup>4+</sup>/Mn<sup>3+</sup> and Ce<sup>3+</sup>/Ce<sup>4+</sup> would also increase with increasing Mn and Ce loading value. A cloud of electrons would shift between the redox cycles of Mn<sup>4+</sup> ↔ Mn<sup>3+</sup> and Ce<sup>3+</sup> ↔ Ce<sup>4+</sup> through the CNFs carbon-based framework, which benefits the Hg<sup>0</sup> oxidation process.

The XRD patterns of the different sorbents are shown in Figure 2. The raw CNFs contained two kinds of carbon structures [30]: graphite 2H (2θ = 25.91°) and common carbon (2θ = 42.49°), of which the graphite 2H was formed by the convolution of two layers of graphene. Graphene has a high degree of graphitization, which facilitates electron transferal through the CNF framework. In addition, Ni crystallization peaks were observed in raw CNFs due to residual Ni catalyst during CNF production. However, the Hg<sup>0</sup> removal efficiency of raw CNFs was only 16.02% (seen from Figure 3), which indicated that the residual Ni has a very limited impact on the Hg<sup>0</sup> removal efficiency. Hence, the impacts of residual Ni on the Hg<sup>0</sup> removal performance can be ignored in this study. It is worth noting that the XRD peak intensity changed significantly after ultrasonic oxidation treatment. The peak intensity of graphite 2H of the CNFs(OX) was much higher than that of raw CNFs, which was owing to the removal of ash content on the raw CNFs' surface during the ultrasonic purification treatment process and the exposure of the graphene phase. For the metal-oxide-loaded samples, the crystal phase ascribed to MnO<sub>x</sub> or CeO<sub>x</sub> was not observed when Mn and Ce loading increased from 6% to 15%, suggesting that MnO<sub>x</sub> and CeO<sub>2</sub> species were well dispersed on the CNFs(OX) surface in amorphous states [22]. A slight crystal phase ascribed to MnO<sub>2</sub> was observed from 18%MnO<sub>x</sub>-18%CeO<sub>2</sub>/CNFs(OX), indicating the aggregation of MnO<sub>x</sub>. The results also demonstrated that the highly dispersed threshold value of the metal oxides on the CNFs(OX) support was about 30%, which is higher than those on other supports. The specific surface area, oxygen-containing functional groups, and the intensity of graphite 2H peak were all enhanced after the ultrasonic oxidation treatment of CNFs, which also facilitated the dispersion and anchoring of active metals.

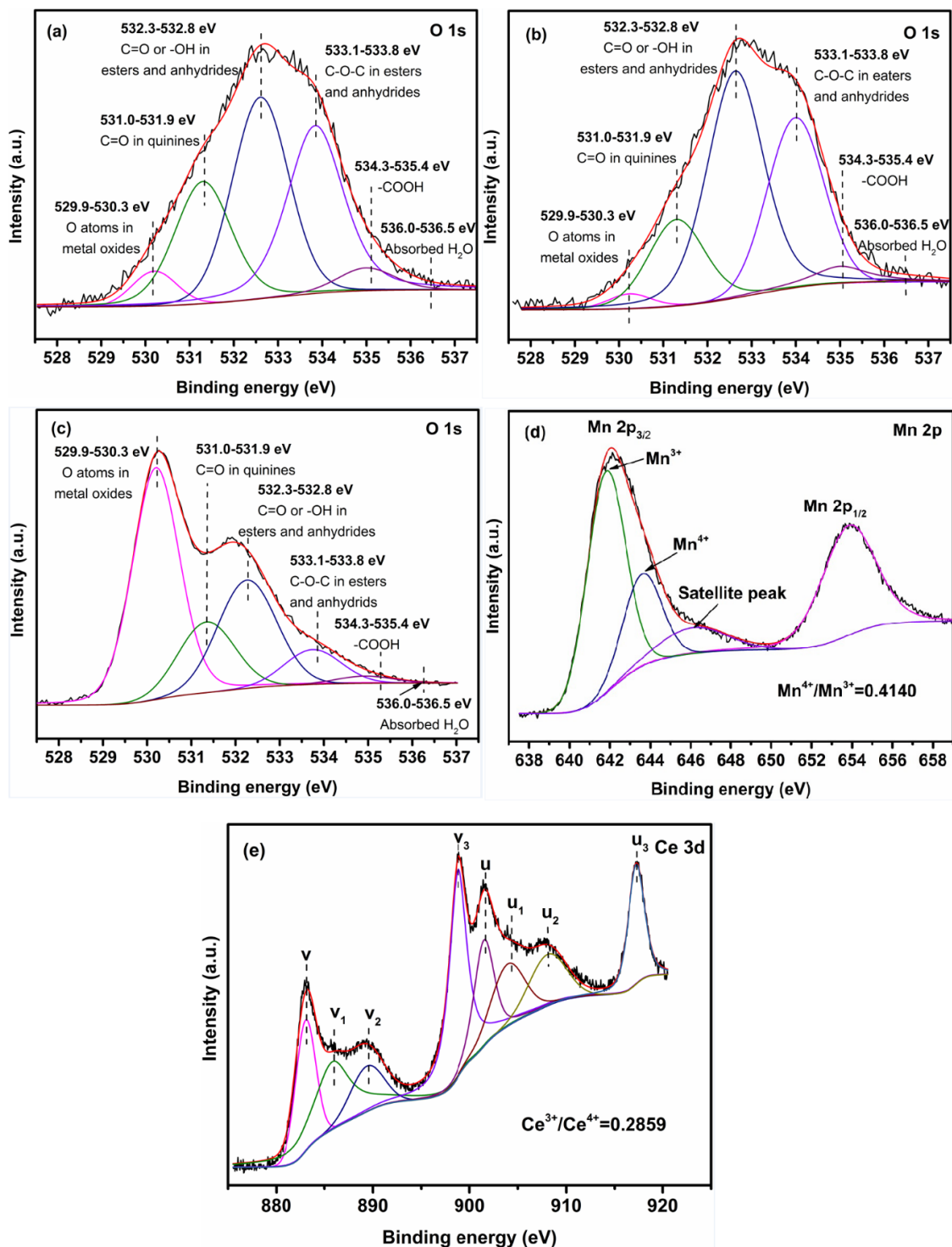


**Figure 1.** O 1s XPS spectra of (a) carbon nanofibers (CNFs) and (b) CNFs(OX). XPS spectra of (c) O 1s, (d) Mn 2p, and (e) Ce 3d for 15%MnO<sub>x</sub>-15%CeO<sub>2</sub>/CNFs(OX).

The micromorphology of the CNFs and the dispersion of MnO<sub>x</sub>-CeO<sub>2</sub> on the surface of the support were evaluated, as shown in Figure 3. As shown in Figure 3a,b, the SEM image of the raw CNFs and 15%MnO<sub>x</sub>-15%CeO<sub>2</sub>/CNFs(OX) showed a homogeneous morphology of cross-linked nanofibers of about 100 nm in diameter. It is clearly observed that the MnO<sub>x</sub> and CeO<sub>2</sub> have been homogeneously dispersed on the support, as shown in Figure 3c.



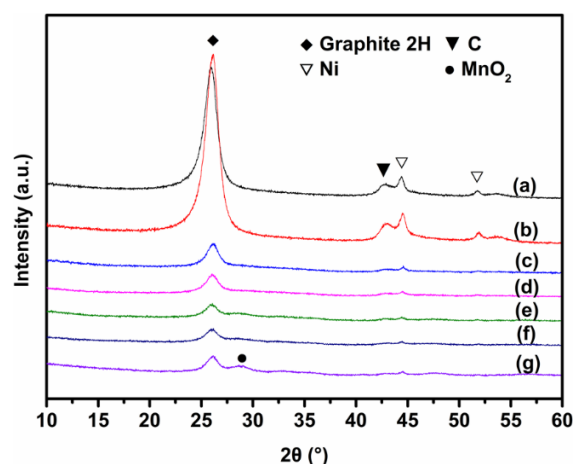


**Figure 2.** XRD patterns of the samples. (a) CNFs; (b) CNFs(OX); (c) 6%MnO<sub>x</sub>–6%CeO<sub>2</sub>/CNFs(OX); (d) 9%MnO<sub>x</sub>–9%CeO<sub>2</sub>/CNFs(OX); (e) 12%MnO<sub>x</sub>–12%CeO<sub>2</sub>/CNFs(OX); (f) 15%MnO<sub>x</sub>–15%CeO<sub>2</sub>/CNFs(OX); (g) 18%MnO<sub>x</sub>–18%CeO<sub>2</sub>/CNFs(OX).

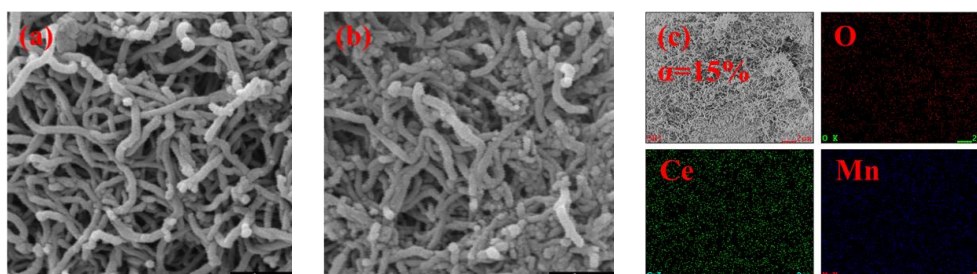


**Figure 3.** Micromorphology of the (a) CNFs and (b) 15%MnO<sub>x</sub>–15%CeO<sub>2</sub>/CNFs(OX), and the EDS mapping of the elements of 15%MnO<sub>x</sub>–15%CeO<sub>2</sub>/CNFs(OX).

**Table 3.** Mercury capacity of the sorbents ( $Q/M = 300,000 \text{ mL} \cdot \text{h}^{-1} \cdot \text{g}^{-1}$ ).

| $\alpha$ | Capacity ( $\mu\text{g} \cdot \text{g}^{-1}$ ) |
|----------|------------------------------------------------|
| 12%      | $74.8 \pm 1.7$                                 |
| 15%      | $118.4 \pm 2.3$                                |
| 18%      | $54.1 \pm 1.2$                                 |

### 3.2. Influence of Loading Value and Reaction Temperature on Hg<sup>0</sup> Removal Performance

Figure 4 shows the experimental results of Set I testing. The Hg<sup>0</sup> removal efficiency of the raw CNFs was only 16.02%. Therefore, the effect of residual Ni in the raw CNFs on their Hg<sup>0</sup> removal efficiency could be ignored. The Hg<sup>0</sup> removal efficiency of CNFs(OX) slightly increased to 18.73%. The increase in the Hg<sup>0</sup> removal efficiency of CNFs(OX) was probably owing to the increase of the specific surface area and the content of surface oxygen-containing functional groups, which enhanced the physicochemical adsorption of Hg<sup>0</sup>. Meanwhile, the Hg<sup>0</sup> removal efficiency increased consistently as the loading value increased from 6% to 15%; however, the efficiency of 18%MnO<sub>x</sub>–18%CeO<sub>2</sub>/CNFs(OX) slightly decreased. This suggested that the optimal loading value for the MnO<sub>x</sub>–CeO<sub>2</sub>/CNFs(OX) sorbent was 15%. This is consistent with the XRD results. The decrease in Hg<sup>0</sup> removal efficiency for 18%MnO<sub>x</sub>–18%CeO<sub>2</sub>/CNFs(OX) was ascribed to the agglomeration of excessive MnO<sub>2</sub>, which resulted in insufficient use of Mn active components.

The Hg<sup>0</sup> removal efficiencies of individual Mn or Ce supported on CNFs(OX) were also tested. As shown in Figure 4, the Hg<sup>0</sup> removal efficiency of 30%Mn/CNFs(OX) was 80.64%, while it was 64.69% for 30%Ce/CNFs(OX). Both of these results were lower than that of 15%MnO<sub>x</sub>–15%CeO<sub>2</sub>/CNFs(OX). The results further demonstrated that Mn and Ce have synergistic effects, consistent with a previous

study [16,19,22]. Meanwhile, the  $\text{Hg}^0$  removal performance of the oxidized-activated-carbon-supported Mn and Ce sorbent (15%MnO<sub>x</sub>–15%CeO<sub>2</sub>/AC(OX)) was also investigated. It was apparent that CNFs(OX) was a better support of MnO<sub>x</sub>–CeO<sub>2</sub> for  $\text{Hg}^0$  removal. The mercury capacities of the sorbents ( $\alpha = 12\%$ , 15% and 18%) are listed in Table 3. In the present study, the  $\text{Hg}^0$  capacity was defined as the amount of  $\text{Hg}^0$  adsorbed per mass of sorbent when  $\text{Hg}^0$  breakthrough reached only 1%.

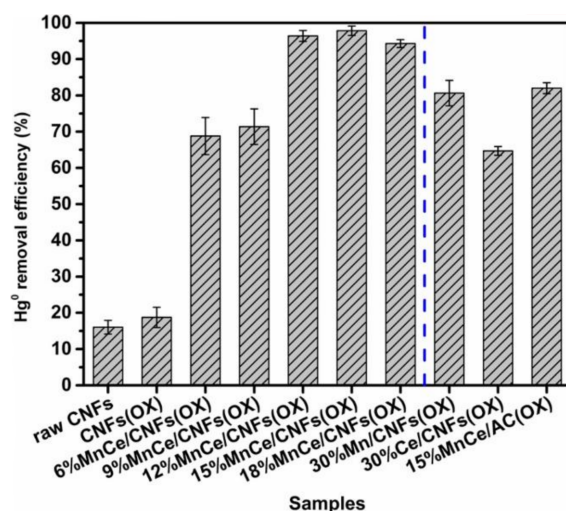


**Figure 4.**  $\text{Hg}^0$  removal efficiency over different samples under a  $\text{N}_2 + 6\%\text{O}_2$  atmosphere at 170 °C. Reaction time for each test was 9 h.

Therefore, subsequent studies were carried out with 15%MnO<sub>x</sub>–15%CeO<sub>2</sub>/CNFs(OX). As shown in Figure 5, the influence of reaction temperature on the  $\text{Hg}^0$  removal performance was investigated. The observation indicated that the optimal reaction temperature for 15%MnO<sub>x</sub>–15%CeO<sub>2</sub>/CNFs(OX) sorbent was 120 °C. It should be noted that over 90% of the  $\text{Hg}^0$  was removed by 15%MnO<sub>x</sub>–15%CeO<sub>2</sub>/CNFs(OX) sorbent in the relatively broad temperature window of 120–220 °C.

In order to evaluate the performance of our sorbents, it was compared with other Mn-based or Ce-based sorbents in some of the published literature [16,19,22,23]. All the results were selected under similar experimental conditions and tested under a  $\text{N}_2 + \text{O}_2$  atmosphere. The ratios of total gas flow rate to sorbent mass in different studies were converted into Q/M. As seen from a general view in Table S2, under similar  $\text{N}_2 + \text{O}_2$  atmosphere and Q/M experimental conditions, the sorbent in the present study exhibited relatively superior activity.

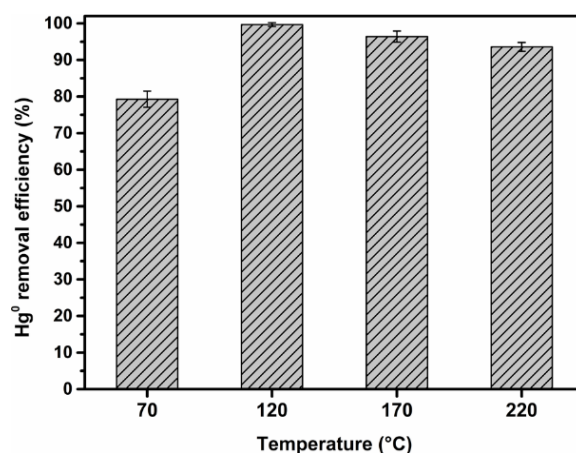


**Figure 5.**  $\text{Hg}^0$  removal efficiency of 15%MnO<sub>x</sub>–15%CeO<sub>2</sub>/CNFs(OX) under a  $\text{N}_2 + 6\%\text{O}_2$  atmosphere at different temperatures. Reaction time for each test was 9 h.

### 3.3. $\text{Hg}^0$ Removal Mechanism Analysis

Figure 6 shows the analysis of the  $\text{Hg}^0$  removal process under a  $\text{N}_2 + 6\%\text{O}_2$  atmosphere by the  $15\%\text{MnO}_x-15\%\text{CeO}_2/\text{CNFs}(\text{OX})$  sorbent. The  $\text{Hg}^0$  in flue gas was almost totally removed by the sorbent during the 9 h reaction. Inset picture (a) displays the Hg-TPD profile of the spent sorbent. Two main desorption peaks were observed in the temperature range of 200–300 °C, indicating that  $\text{Hg}^0$  was mainly captured on the sorbent surface via chemical adsorption [12,31]. By integrating the Hg-TPD profile, ~81% of total  $\text{Hg}^0$  was adsorbed on the sorbent, while the rest of the  $\text{Hg}^0$  was removed by catalytic oxidation and released to the flue gas, as shown in inset picture (b).

Figure 7 shows the XPS analysis of O 1s, Mn 2p, and Ce 3d with spent  $15\%\text{MnO}_x-15\%\text{CeO}_2/\text{CNFs}(\text{OX})$ . For spent  $15\%\text{MnO}_x-15\%\text{CeO}_2/\text{CNFs}(\text{OX})$ , the ratio of  $\text{Mn}^{4+}/\text{Mn}^{3+}$  was 0.3633, and the ratio of  $\text{Ce}^{3+}/\text{Ce}^{4+}$  was 0.2371. Both of these values are lower than those of the fresh sorbent, so it can be inferred that  $\text{Mn}^{4+}$  and  $\text{Ce}^{3+}$  participated in the catalytic adsorption and oxidation of  $\text{Hg}^0$ .

In summary, for  $15\%\text{MnO}_x-15\%\text{CeO}_2/\text{CNFs}(\text{OX})$ , two approaches of adsorption and catalytic oxidation existed for  $\text{Hg}^0$  removal, of which the chemical adsorption approach occupied the main proportion. The active components such as active oxygen species,  $\text{Mn}^{4+}$  species, and  $\text{Ce}^{3+}$  species greatly benefited the chemical adsorption and oxidation of  $\text{Hg}^0$ . The relatively high loading capacity of the highly dispersed Mn and Ce provided more active components for  $\text{Hg}^0$  removal.

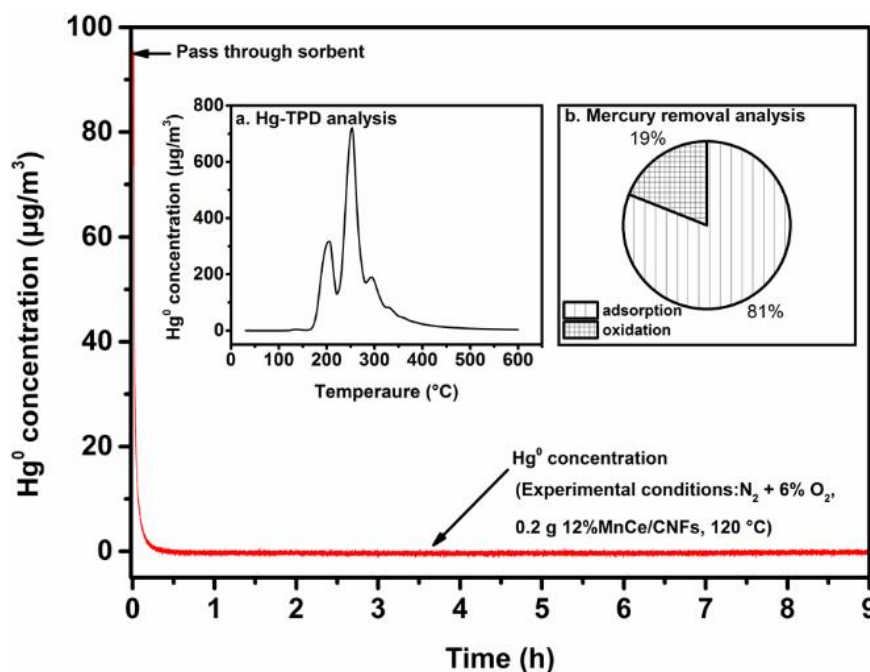


**Figure 6.**  $\text{Hg}^0$  concentration versus reaction time for  $15\%\text{MnO}_x-15\%\text{CeO}_2/\text{CNFs}(\text{OX})$ . Inset pictures: (a) Hg-TPD analysis of spent  $15\%\text{MnO}_x-15\%\text{CeO}_2/\text{CNFs}(\text{OX})$ ; (b) Balance analysis of  $15\%\text{MnO}_x-15\%\text{CeO}_2/\text{CNFs}(\text{OX})$ .



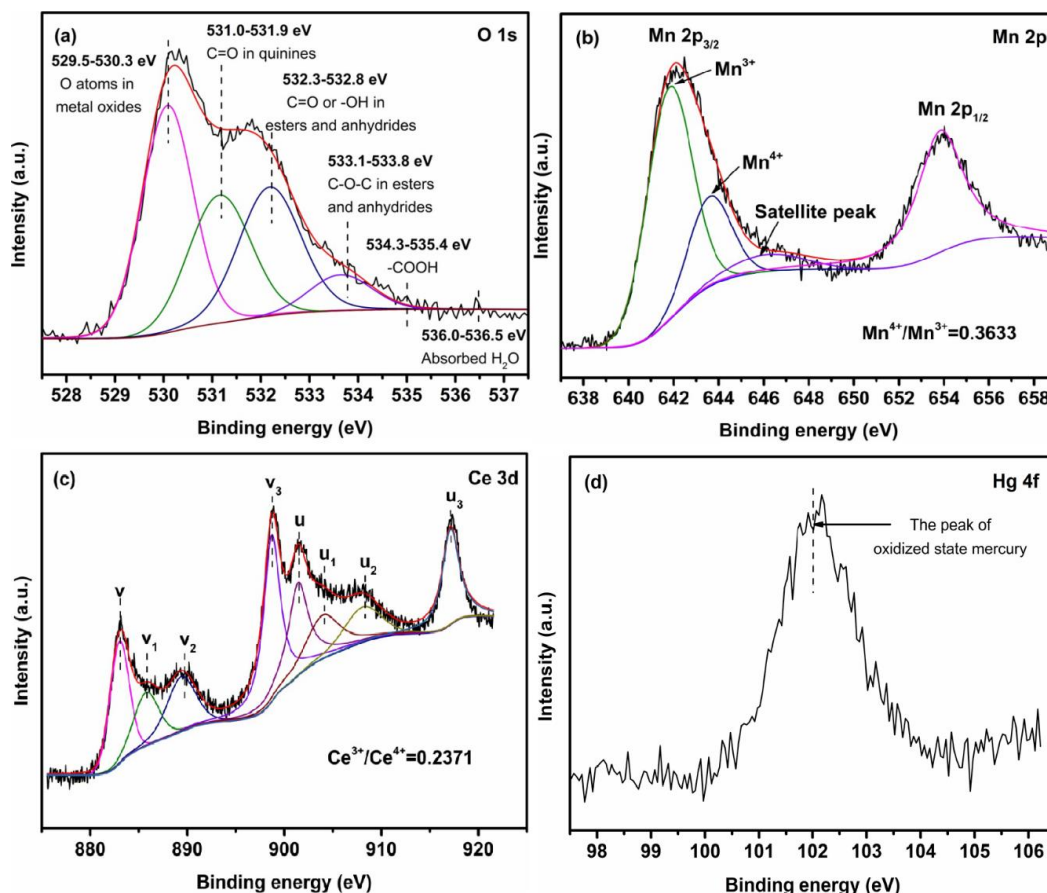


**Figure 7.** The (a) O 1s, (b) Mn 2p, (c) Ce 3d, and (d) Hg 4f XPS spectra of the spent 15%MnO<sub>x</sub>–15%CeO<sub>2</sub>/CNFs(OX).

### 3.4. Influence of Individual Flue Gas Components on Hg<sup>0</sup> Removal Performance

Figure 8 shows the influences of CO<sub>2</sub>, O<sub>2</sub>, SO<sub>2</sub>, NO, and H<sub>2</sub>O on the Hg<sup>0</sup> removal performance of 15%MnO<sub>x</sub>–15%CeO<sub>2</sub>/CNFs(OX) at 120 °C. The Hg<sup>0</sup> removal efficiency was 53.48% under a pure N<sub>2</sub> atmosphere, while it was 46.08% under a N<sub>2</sub> + 12%CO<sub>2</sub> atmosphere. This indicated that CO<sub>2</sub> had a slight inhibitory effect on Hg<sup>0</sup> removal performance, which may be caused by competitive adsorption of Hg<sup>0</sup> and CO<sub>2</sub> on the sorbent. The Hg<sup>0</sup> removal efficiency increased to 81.94% when the O<sub>2</sub> concentration was 3% (balanced N<sub>2</sub>), while it was 99.6% when the O<sub>2</sub> concentration increased to 6%. The observation indicated that O<sub>2</sub> played an important role in the Hg<sup>0</sup> removal process. In this study, a large amount of Ce was well dispersed on the support, which greatly facilitated the transport of O<sub>2</sub> in the flue gas to the sorbent surface. Moreover, the active oxygen content in CeO<sub>2</sub> favored the transformation of Mn<sup>3+</sup> to Mn<sup>4+</sup> [22], and the increase of the Mn<sup>4+</sup>/Mn<sup>3+</sup> ratio was beneficial to the removal of Hg<sup>0</sup> [32].

When SO<sub>2</sub> was added into the N<sub>2</sub> flow, the Hg<sup>0</sup> removal efficiency decreased significantly. However, the negative influence of SO<sub>2</sub> on Hg<sup>0</sup> removal performance was relieved in the presence of O<sub>2</sub>. As shown in Figure 7, the Hg<sup>0</sup> removal efficiency was 60.52% under the atmosphere of N<sub>2</sub> + 6%O<sub>2</sub> + 500 ppm SO<sub>2</sub>. When the SO<sub>2</sub> concentration further increased to 1000 ppm and 1500 ppm, the Hg<sup>0</sup> removal efficiency decreased to 50.95% and 46.73%, respectively. The influence of SO<sub>2</sub> observed in the present study was consistent with that observed in previous studies [28]. The consumption of active oxygen and the reaction of Mn with SO<sub>2</sub> on the sorbent surface may account for the inhibition effects. The Hg<sup>0</sup> removal efficiency sharply reached 90.37% when 100 ppm NO was added into the N<sub>2</sub> atmosphere. Besides this, when the NO concentration was further increased to 200 ppm and 300 ppm, the Hg<sup>0</sup> removal efficiency increased to 97.33% and 98.17%, respectively. Furthermore, NO could

promote the  $\text{Hg}^0$  removal efficiency in the absence and presence of  $\text{O}_2$ . We believe that active oxygen on the sorbent surface promoted the conversion of NO to active nitrites, which were beneficial for  $\text{Hg}^0$  oxidation [33]. Water vapor ( $\text{H}_2\text{O}$ ) exhibited only a slight inhibition effect on the  $\text{Hg}^0$  removal performance, suggesting that the sorbent could be used in low-temperature coal-fired flue gas, which always contains  $\text{H}_2\text{O}$ .

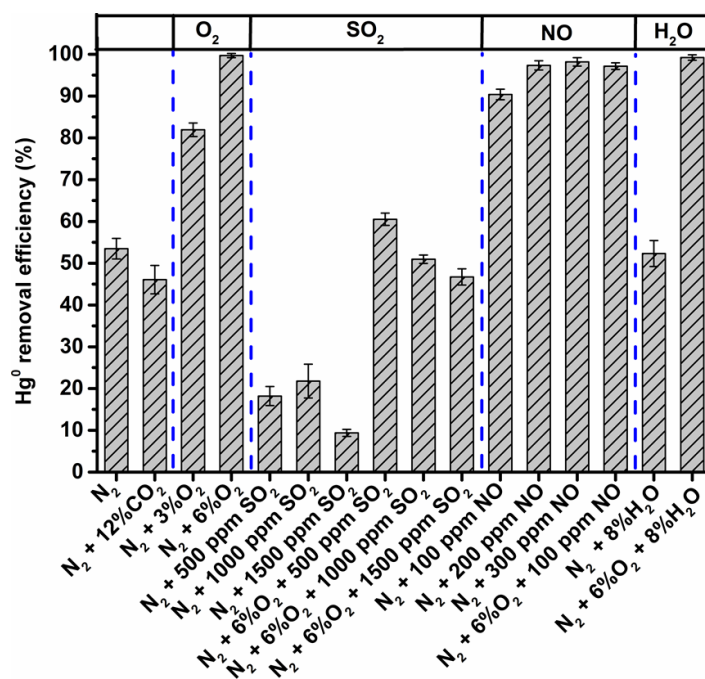


**Figure 8.**  $\text{Hg}^0$  removal efficiency of  $15\% \text{MnO}_x-15\% \text{CeO}_2/\text{CNFs}(\text{OX})$  under different individual flue gas components at  $120^\circ \text{C}$ .

### 3.5. Possible Application Mode of the Sorbent

To reduce anthropogenic mercury emissions into the environment, more than 128 nations have approved the Minamata Convention on Mercury until 4 November 2018. As one of the most important anthropogenic sources, coal-fired power plants should make efforts to reduce their  $\text{Hg}^0$  emissions. The existing air pollution control devices cannot efficiently remove the  $\text{Hg}^0$ , so some new devices are needed to control the  $\text{Hg}^0$  emissions. A possible application mode of the sorbent for  $\text{Hg}^0$  control from coal-fired flue gas is shown in Figure 9. One option is to inject the mercury sorbent into the flue gas downstream of the electrostatic precipitator (ESP) and upstream of a small fabric filter (FF), as shown in Figure 9a. In this way, an injector and an FF should be introduced to the flue gas clean system. The sorbent will capture  $\text{Hg}^0$  in the flue gas and will be then collected by the FF so as to achieve separation from the fly ash. In this way, the spent sorbent will probably be regenerated. In addition, the FF can efficiently remove fine particulate matter ( $\text{PM}_{2.5}$ ) simultaneously. The other option is to make use of a fixed adsorption bed, as shown in Figure 9b. The sorbent could be shaped into a honeycomb or plate, like the selective catalytic reduction (SCR) catalysts.

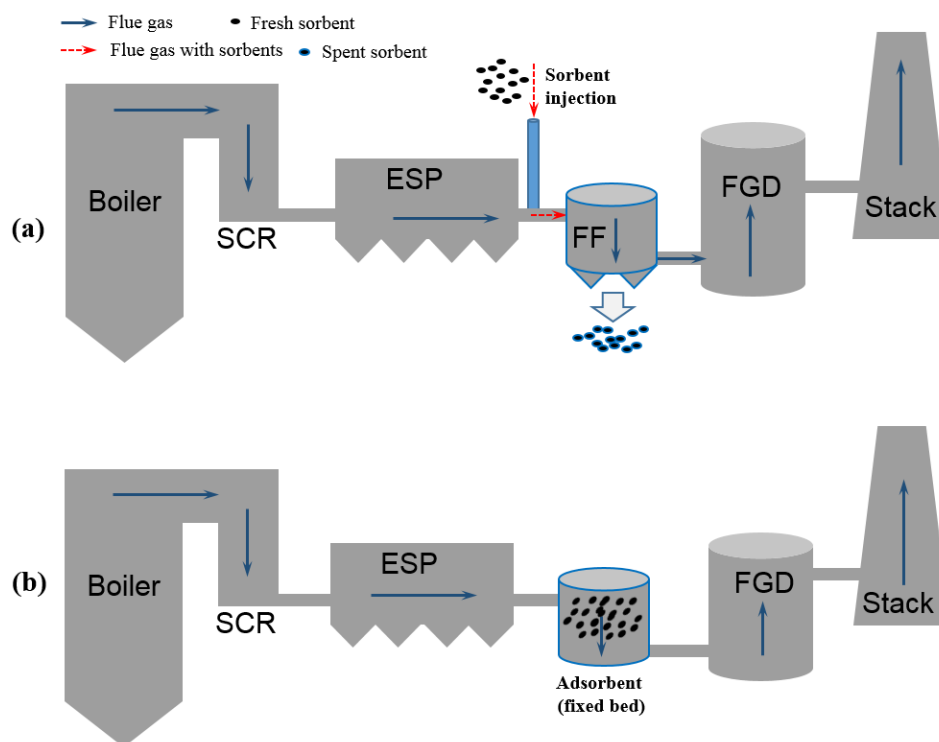


**Figure 9.** Possible application mode of the sorbent: (a) powder adsorbent injection; (b) fixed adsorbent bed.

#### 4. Conclusions

$\text{Hg}^0$  removal performance experiments were carried out on  $\text{MnO}_x\text{-CeO}_2$ -modified CNF sorbents in this study. The results showed that the  $\text{Hg}^0$  removal efficiency increased continuously as the loading value increased from 6% to 15%. Moreover, the sorbents exhibited superior performance in a wide temperature range (120–220 °C). Compared with those of some other supports, the well-dispersed Mn–Ce mixed oxide loading amount on CNFs was improved. The  $\text{Hg}^0$  removal performance of this sorbent was clearly enhanced by  $\text{O}_2$  and NO in the flue gas.  $\text{SO}_2$  inhibited the removal activity, and resistance to  $\text{SO}_2$  should be investigated in future work. Overall, this study showed that CNFs could serve as a good sorbent support for  $\text{MnO}_x\text{-CeO}_2$  mixed oxides.

**Supplementary Materials:** The followings are available online at <http://www.mdpi.com/2076-3417/8/12/2501/s1>. The sorbent preparation and characterization are described in the Supplementary Materials. Two tables are also presented in the file. Table S1. Experimental conditions. Table S2. A comparison of the  $\text{Hg}^0$  removal efficiency in this study and those of other Mn–Ce-based composites reported in the literature.

**Author Contributions:** Y.X., Z.L. and Y.Z. performed the experiments; Z.Z. wrote the paper.

**Funding:** This research was funded by the National Key R&D Program of China [2018YFB0605200], the China Postdoctoral Science Foundation funded project [2018T110762] and Jiangxi Key R&D Program [20171ACG70012]. And The APC was funded by [20171ACG70012].

**Acknowledgments:** We appreciate the support from the Analytical and Testing Center at Huazhong University of Science & Technology.

**Conflicts of Interest:** The authors declare no conflict of interest.

#### References

1. Doney, S.C. The Growing Human Footprint on Coastal and Open-Ocean Biogeochemistry. *Science* **2010**, *328*, 1512–1516. [CrossRef] [PubMed]
2. Wilcox, J.; Rupp, E.; Ying, S.C.; Lim, D.-H.; Negreira, A.S.; Kirchofer, A.; Feng, F.; Lee, K. Mercury adsorption and oxidation in coal combustion and gasification processes. *Int. J. Coal Geol.* **2012**, *90–91*, 4–20. [CrossRef]

3. Xu, M.; Yan, R.; Zheng, C.; Qiao, Y.; Han, J.; Sheng, C. Status of trace element emission in a coal combustion process: A review. *Fuel Process. Technol.* **2004**, *85*, 215–237. [[CrossRef](#)]
4. Hower, J.C.; Senior, C.L.; Suuberg, E.M.; Hurt, R.H.; Wilcox, J.L.; Olson, E.S. Mercury capture by native fly ash carbons in coal-fired power plants. *Prog. Energy Combust. Sci.* **2010**, *36*, 510–529. [[CrossRef](#)] [[PubMed](#)]
5. Xu, M.; Qiao, Y.; Zheng, C.; Li, L.; Liu, J. Modeling of homogeneous mercury speciation using detailed chemical kinetics. *Combust. Flame* **2003**, *132*, 208–218. [[CrossRef](#)]
6. Zhou, Z.-J.; Liu, X.-W.; Zhao, B.; Chen, Z.-G.; Shao, H.-Z.; Wang, L.-L.; Xu, M.-H. Effects of existing energy saving and air pollution control devices on mercury removal in coal-fired power plants. *Fuel Process. Technol.* **2015**, *131*, 99–108. [[CrossRef](#)]
7. Lee, S.J.; Seo, Y.-C.; Jang, H.-N.; Park, K.-S.; Baek, J.-I.; An, H.-S.; Song, K.-C. Speciation and mass distribution of mercury in a bituminous coal-fired power plant. *Atmos. Environ.* **2006**, *40*, 2215–2224. [[CrossRef](#)]
8. Padak, B.; Wilcox, J. Understanding mercury binding on activated carbon. *Carbon* **2009**, *47*, 2855–2864. [[CrossRef](#)]
9. Rupp, E.C.; Wilcox, J. Mercury chemistry of brominated activated carbons-Packed-bed breakthrough experiments. *Fuel* **2014**, *117*, 351–353. [[CrossRef](#)]
10. Li, H.; Li, Y.; Wu, C.-Y.; Zhang, J. Oxidation and capture of elemental mercury over  $\text{SiO}_2\text{-TiO}_2\text{-V}_2\text{O}_5$  catalysts in simulated low-rank coal combustion flue gas. *Chem. Eng. J.* **2011**, *169*, 186–193. [[CrossRef](#)]
11. Kamata, H.; Ueno, S.-I.; Naito, T.; Yukimura, A. Mercury Oxidation over the  $\text{V}_2\text{O}_5(\text{WO}_3)/\text{TiO}_2$  Commercial SCR Catalyst. *Ind. Eng. Chem. Res.* **2008**, *47*, 8136–8141. [[CrossRef](#)]
12. Yang, J.; Zhao, Y.; Zhang, J.; Zheng, C. Regenerable Cobalt Oxide Loaded Magnetosphere Catalyst from Fly Ash for Mercury Removal in Coal Combustion Flue Gas. *Environ. Sci. Technol.* **2014**, *48*, 14837–14843. [[CrossRef](#)] [[PubMed](#)]
13. Li, H.; Zhu, L.; Wu, S.; Liu, Y.; Shih, K. Synergy of  $\text{CuO}$  and  $\text{CeO}_2$  combination for mercury oxidation under low-temperature selective catalytic reduction atmosphere. *Int. J. Coal Geol.* **2017**, *170*, 69–76. [[CrossRef](#)]
14. Yang, Y.; Liu, J.; Wang, Z.; Liu, F. Heterogeneous reaction kinetics of mercury oxidation by  $\text{HCl}$  over  $\text{Fe}_2\text{O}_3$  surface. *Fuel Process. Technol.* **2017**, *159*, 266–271. [[CrossRef](#)]
15. Zhou, Z.; Liu, X.; Hu, Y.; Liao, Z.; Cheng, S.; Xu, M. An efficient sorbent based on  $\text{CuCl}_2$  loaded  $\text{CeO}_2\text{-ZrO}_2$  for elemental mercury removal from chlorine-free flue gas. *Fuel* **2018**, *216*, 356–363. [[CrossRef](#)]
16. He, C.; Shen, B.; Chen, J.; Cai, J. Adsorption and Oxidation of Elemental Mercury over  $\text{Ce-MnO}_x/\text{Ti-PILCs}$ . *Environ. Environ. Sci. Technol.* **2014**, *48*, 7891–7898. [[CrossRef](#)]
17. Zhou, Z.; Liu, X.; Zhao, B.; Shao, H.; Xu, Y.; Xu, M. Elemental mercury oxidation over manganese-based perovskite-type catalyst at low temperature. *Chem. Eng. J.* **2016**, *288*, 701–710. [[CrossRef](#)]
18. Li, H.; Wu, C.-Y.; Li, Y.; Zhang, J.  $\text{CeO}_2\text{-TiO}_2$  catalysts for catalytic oxidation of elemental mercury in low-rank coal combustion flue gas. *Environ. Sci. Technol.* **2011**, *45*, 7394–7400. [[CrossRef](#)]
19. Li, H.; Wu, C.-Y.; Li, Y.; Zhang, J. Superior activity of  $\text{MnO}_x\text{-CeO}_2/\text{TiO}_2$  catalyst for catalytic oxidation of elemental mercury at low flue gas temperatures. *Appl. Catal. B Environ.* **2012**, *111–112*, 381–388. [[CrossRef](#)]
20. Devaiah, D.; Reddy, L.H.; Park, S.-E.; Reddy, B.M. Ceria–zirconia mixed oxides: Synthetic methods and applications. *Catal. Rev.* **2018**, *60*, 177–277. [[CrossRef](#)]
21. He, J.; Reddy, G.K.; Thiel, S.W.; Smirniotis, P.G.; Pinto, N.G. Simultaneous Removal of Elemental Mercury and NO from Flue Gas Using  $\text{CeO}_2$  Modified  $\text{MnO}_x/\text{TiO}_2$  Materials. *Energy Fuels* **2013**, *27*, 4832–4839. [[CrossRef](#)]
22. Xie, Y.; Li, C.; Zhao, L.; Zhang, J.; Zeng, G.; Zhang, X.; Zhang, W.; Tao, S. Experimental study on  $\text{Hg}^0$  removal from flue gas over columnar  $\text{MnO}_x\text{-CeO}_2$ /activated coke. *Appl. Surf. Sci.* **2015**, *333*, 59–67. [[CrossRef](#)]
23. Wang, P.; Su, S.; Xiang, J.; You, H.; Cao, F.; Sun, L.; Hu, S.; Zhang, Y. Catalytic oxidation of  $\text{Hg}^0$  by  $\text{MnO}_x\text{-CeO}_2/\gamma\text{-Al}_2\text{O}_3$  catalyst at low temperatures. *Chemosphere* **2014**, *101*, 49–54. [[CrossRef](#)] [[PubMed](#)]
24. Zhou, J.-H.; Sui, Z.-J.; Zhu, J.; Li, P.; Chen, D.; Dai, Y.-C.; Yuan, W.-K. Characterization of surface oxygen complexes on carbon nanofibers by TPD, XPS and FT-IR. *Carbon* **2007**, *45*, 785–796. [[CrossRef](#)]
25. Xu, H.; Qu, Z.; Zong, C.; Huang, W.; Quan, F.; Yan, N.  $\text{MnO}_x$ /Graphene for the Catalytic Oxidation and Adsorption of Elemental Mercury. *Environ. Sci. Technol.* **2015**, *49*, 6823–6830. [[CrossRef](#)] [[PubMed](#)]
26. Zhang, B.; Xu, P.; Qiu, Y.; Yu, Q.; Ma, J.; Wu, H.; Luo, G.; Xu, M.; Yao, H. Increasing oxygen functional groups of activated carbon with non-thermal plasma to enhance mercury removal efficiency for flue gases. *Chem. Eng. J.* **2015**, *263*, 1–8. [[CrossRef](#)]

27. Mizokawa, T.; Nambu, T.; Fujimori, A.; Fukumura, T.; Kawasaki, M. Electronic structure of the oxide-diluted magnetic semiconductor  $\text{Zn}_{1-x}\text{Mn}_x\text{O}$ . *Phys. Rev. B* **2002**, *65*, 085209. [[CrossRef](#)]
28. Zhou, Z.; Liu, X.; Liao, Z.; Shao, H.; Lv, C.; Hu, Y.; Xu, M. Manganese doped  $\text{CeO}_2\text{-ZrO}_2$  catalyst for elemental mercury oxidation at low temperature. *Fuel Process. Technol.* **2016**, *152*, 285–293. [[CrossRef](#)]
29. Li, H.; Wu, S.; Li, L.; Wang, J.; Ma, W.; Shih, K.  $\text{CuO-CeO}_2/\text{TiO}_2$  catalyst for simultaneous NO reduction and  $\text{Hg}^0$  oxidation at low temperatures. *Catal. Sci. Technol.* **2015**, *5*, 5129–5138. [[CrossRef](#)]
30. Endo, M.; Kim, Y.A.; Hayashi, T.; Yanagisawa, T.; Muramatsu, H.; Ezaka, M.; Terrones, H.; Terrones, M.; Dresselhaus, M.S. Microstructural changes induced in “stacked cup” carbon nanofibers by heat treatment. *Carbon* **2003**, *41*, 1941–1947. [[CrossRef](#)]
31. Xu, H.; Ma, Y.; Huang, W.; Mei, J.; Zhao, S.; Qu, Z.; Yan, N. Stabilization of mercury over Mn-based oxides, Speciation and reactivity by temperature programmed desorption analysis. *J. Hazard. Mater.* **2017**, *321*, 745–752. [[CrossRef](#)] [[PubMed](#)]
32. Li, J.; Yan, N.; Qu, Z.; Qiao, S.; Yang, S.; Guo, Y.; Liu, P.; Jia, J. Catalytic Oxidation of Elemental Mercury over the Modified Catalyst  $\text{Mn}/\alpha\text{-Al}_2\text{O}_3$  at Lower Temperatures. *Environ. Sci. Technol.* **2010**, *44*, 426–431. [[CrossRef](#)] [[PubMed](#)]
33. Zhou, Z.; Liu, X.; Hu, Y.; Xu, J.; Cao, X.E.; Liao, Z.; Xu, M. Investigation on synergistic oxidation behavior of NO and  $\text{Hg}^0$  during the newly designed fast SCR process. *Fuel* **2018**, *225*, 134–139. [[CrossRef](#)]



© 2018 by the authors. Licensee MDPI, Basel, Switzerland. This article is an open access article distributed under the terms and conditions of the Creative Commons Attribution (CC BY) license (<http://creativecommons.org/licenses/by/4.0/>).